bubbles from the electrode surface in time and reduce the overpotential caused by bubbles. In addition, modifying the electrode structure has also become one of the research directions.

Currently, commercial nickel foam is widely used in high-efficiency electrodes [17-20]. However, commercial nickel foam is difficult to balance the specific surface area and bubble transmission resistance. Freeze casting, a low-cost and environmentally friendly method, offers a solution for preparing aligned porous materials [21-23]. Aligned porous materials possess a unique double pore size structure. The large pore size is formed by the growth of ice crystals, enabling efficient gas-liquid transport, while the small pore size is formed by the accumulation of particles to provide sufficient reaction sites. The microstructure and macroscopic structure of the aligned porous materials can be controlled by adjusting freezing parameters during the preparation process [24-26]. In our previous work, we compared the hydrogen evolution performance of nickel foam, nickel fiber felt and aligned porous electrodes. Due to the larger electrochemical active surface area (ECSA) and stronger bubble removal ability, aligned porous electrodes exhibit excellent HER performance [27]. This paper compares the aligned porous electrode prepared using in flake nickel powder and spherical nickel powder, and studies their electrochemical performance and bubble removal ability.

2. MATERIAL AND METHODS

2.1 Preparation of slurry

The spherical nickel powder or flake nickel powder was evenly mixed with thickener, 0.25 wt% (relative to nickel powder) Xanthan gum. Polyvinyl pyrrolidone (PVP) solutions, polyvinyl alcohol (PVA) solutions with both mass fractions of 6% and deionized water were added. The volume fraction of deionized water was 45%. The PVP solution with volume fraction of 15% was used as dispersant and PVA solution with volume fraction of 30% was used as binder. The slurry was dispersed using a planetary ball mill at 150 rpm for 12 hours.

2.2 Fabrication of nickel electrodes

The well-dispersed slurry was evenly coated on a copper substrate using a pipette gun. The sample was placed on a -10 °C freezing platform, and then the frozen sample was transferred to a freeze dryer for 12 hours. The prepared samples were sintered in a tubular furnace under a hydrogen (5%) and argon atmosphere. The temperature was increased at a rate of 5 °C/min from room temperature. The samples were held at 400°C for two hours to remove organic matter, and then the

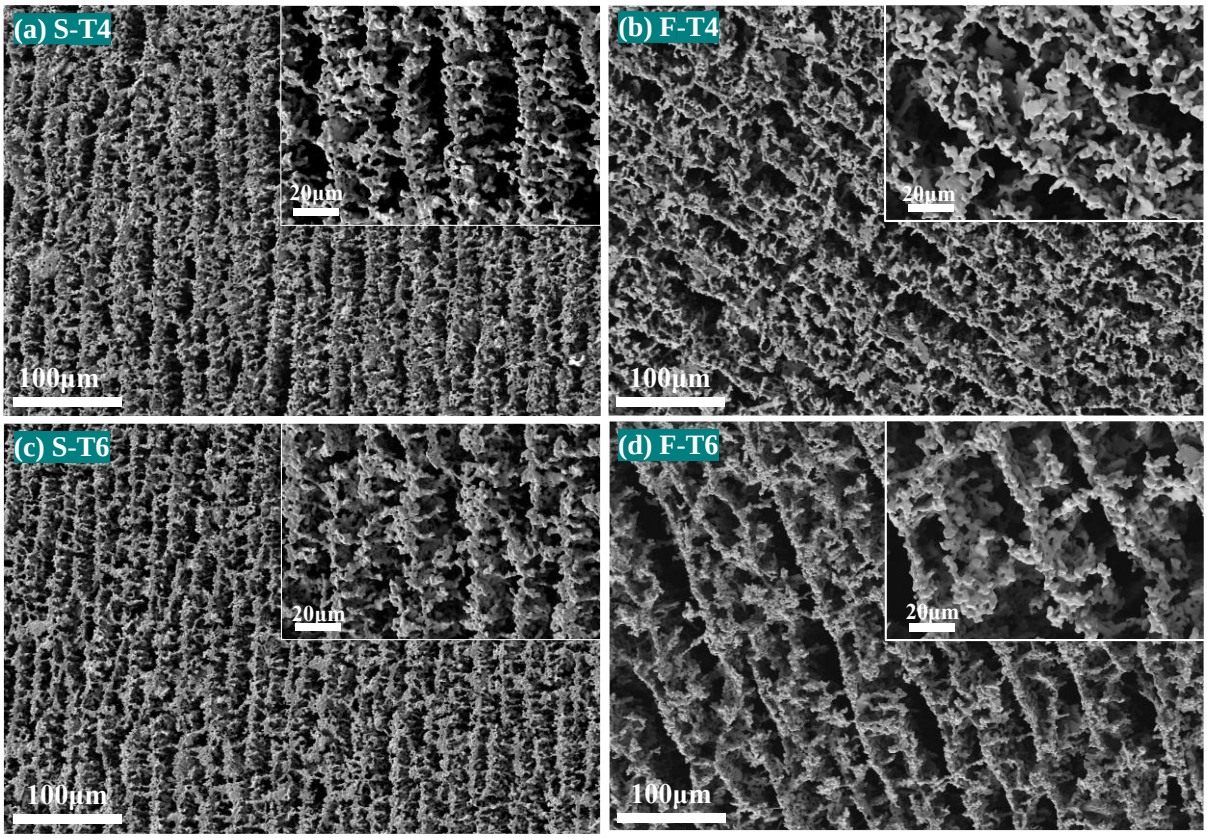

Fig. 1. SEM images of the electrodes with different nickel powders and thicknesses

temperature was slowly lowered to room temperature after being held at 800 °C for two hours. Two types of electrodes with thickness 400 μm (T4) and 600 μm (T6) were prepared, and electrodes were named according to their its thickness and the shape of nickel powder.

2.3 Electrochemical measurement

The electrochemical performance of the prepared porous electrodes was evaluated using the electrochemical workstation CHI660E in a three-electrode system. The working electrode was the prepared porous electrodes (1×1 cm), while the counter electrode was a platinum foil (2×2 cm). The Hg/HgO electrode was used as the reference electrode, and all measured potential was converted to the potential of the relatively reversible hydrogen electrode (RHE). Prior to the actual measurements, cyclic voltammetry (CV) was conducted at a scan rate of 100 mV/s. Linear sweep voltammetry (LSV) was performed at a scanning rate of 1 mV/s, and 95% IR compensation was applied.

3. RESULTS AND DISCUSSION

3.1 Characterization of porous electrodes

Fig. 1 shows the SEM images of the four electrodes. The aligned pores formed by the sublimation of ice crystals and the porous skeleton formed by the accumulation of nickel powder are observed. The skeleton provides the reaction site, and the aligned pores allow the bubbles to escape smoothly. In addition, distinct connections referred to as "bridges" can be observed between the skeletons, and the aligned porous electrode prepared with spherical nickel powder has more derivatives. The average pore size of the electrode was measured by mercury injection method. The average pore size of the electrode prepared by spherical nickel powder was approximately 14 μm, and that of the electrode prepared by flake nickel powder was approximately 17 μm.

3.2 HER performance of porous electrodes

Fig. 2a shows the polarization curves of the four aligned porous electrodes. At low current density, the overpotential of electrodes S-T4 and S-T6, made of spherical nickel powder, is lower compared to electrodes made of flake nickel powder with the same thickness. While the overpotential of S-T4 and S-T6 gradually becomes higher than that of F-T4 and F-T6 with the increase of current density. In addition, the effect of increasing the thickness from 400 μm to 600 μm differs for electrodes prepared by the two kinds of nickel powders. For electrodes prepared by spherical nickel powder, the overpotential of S-T6 is lower than that of S-T4 at low current density. However, as the current gradually increases to about 250 mA/cm^2, the overpotential of both becomes equal. Furthermore, as the current density continues to increase, the overpotential of S-T6 is higher than that of S-T4. On the other hand, for electrodes prepared with flake nickel powder, the overpotential of F-T6 is lower than that of F-T4 within the tested range. Fig. 2b shows the overpotential of each electrode at different current density. The smallest η_{25} obtained by S-T6 is 125 mV, while the smallest values of η_{100}, η_{200}, and η_{300} are obtained by F-T6, measuring 198 mV, 228 mV, and 254 mV, respectively.

Fig. 3 shows the Tafel slope for the four aligned porous electrodes. The Tafel slope reflects the reaction kinetics of HER, and the lower slope indicates the faster the reaction process. The slopes of F-T4 and F-T6 are 85.2

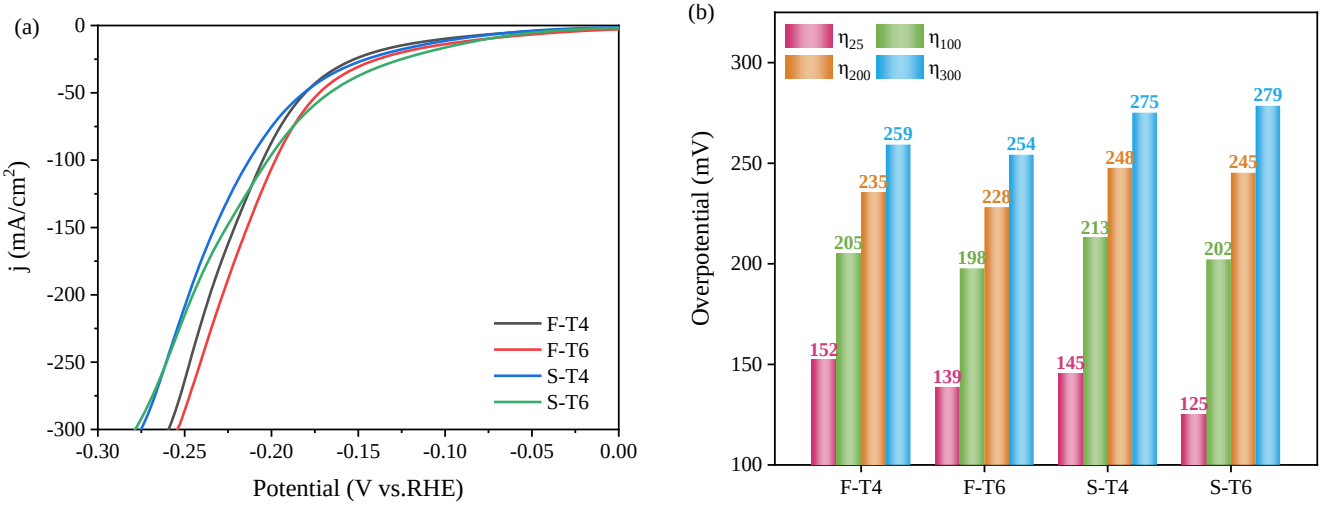

Fig. 2. (a) Polarization curves of each electrode for HER. (b) The η_{25}, η_{100}, η_{200}, and η_{300} with different aligned porous electrodes

mV/dec and 86.5 mV/dec, respectively, and they show little variation with thickness. The slopes of S-T4 and S-T6 are 116.4 mV/dec and 125.2 mV/dec, respectively, and these slopes increase with the increase of thickness. Notably, the slope of the aligned porous electrode prepared by spherical nickel powder is significantly higher than that of the electrode prepared with flake nickel powder. This indicates that the morphology of the nickel powder affects the reaction rate of the electrode.

The electrochemically active surface area (ECSA) of

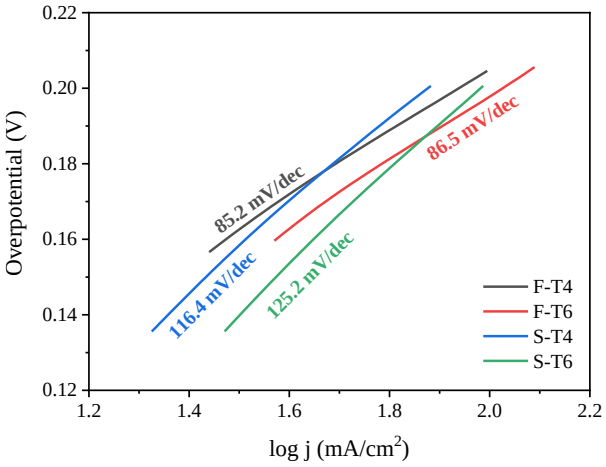

Fig 3. Tafel plots of aligned porous electrodes for HER

the electrode reflects the actual area of the electrode participating in the electrochemical reaction, which is measured using the double layer capacitance (C_{dl}) method in this study. The CV scan range is 0.7 to 0.8 V, and scan rate used is 10, 20, 40, 60, 80 and 100 mV/s. Fig.

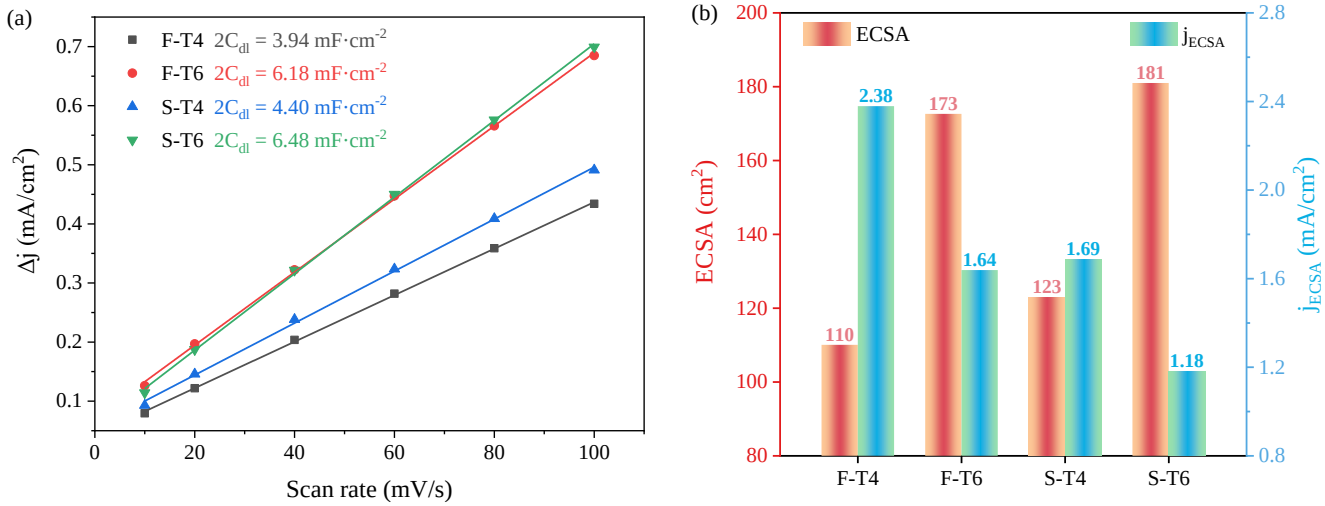

Fig. 4. The curves of current density at 0.75V against sweeping rate. (b) ECSA and j_{ECSA} at 250 mV of each electrode

4a shows the current density difference and scanning rate at 0.75V, and its curve slope represents 2Cdl. The

results indicate that ECSA increases with the thickness of the porous electrode, and the aligned porous electrode prepared by spherical nickel powder exhibits a larger ECSA. However, the hydrogen evolution performance of the aligned porous electrode prepared with spherical nickel powder decreases with the increase of current density, suggesting a greater influence from bubbles. Fig. 4b also shows the ECSA normalized current density (j_{ECSA}) for each electrode at 250 mV. F-T4 achieves the maximum value of 2.38 mA/cm^2, and the j_{ECSA} of F-T6 is 1.64 mA/cm^2, slightly lower than that of S-T4. Furthermore, j_{ECSA} decreases with the increase of electrode thickness, indicating a reduction in material utilization efficiency as the thickness increases.

3.3 Effect of morphology of nickel powder on bubble removal capability

In order to investigate the difference of hydrogen evolution performance of aligned porous electrodes prepared with different morphology of nickel powder, we conducted a quantitative analysis of the bubble removal ability of each electrode. Fig. 5a shows the overpotential of each aligned porous electrode at j_{ECSA} of 0.2, 0.4, 0.5, and 1.0 mA/cm^2. Based on the Tafel formula (i.e., $\eta = a + b \log j$), for the same electrode in an ideal process, there are:

$$\Delta\eta_1 = \eta_{jECSA=0.4} - \eta_{jECSA=0.2} = b \log 2 \quad (1)$$

$$\Delta\eta_2 = \eta_{jECSA=1.0} - \eta_{jECSA=0.5} = b \log 2 \quad (2)$$

This implies that $\Delta\eta_1$ and $\Delta\eta_2$ should be equal. However, in actual processes, the measured overpotential includes the contribution from bubbles, and therefore, they are generally not equal. Since $\Delta\eta_1$ and $\Delta\eta_2$ contain the same part of overpotential reflecting

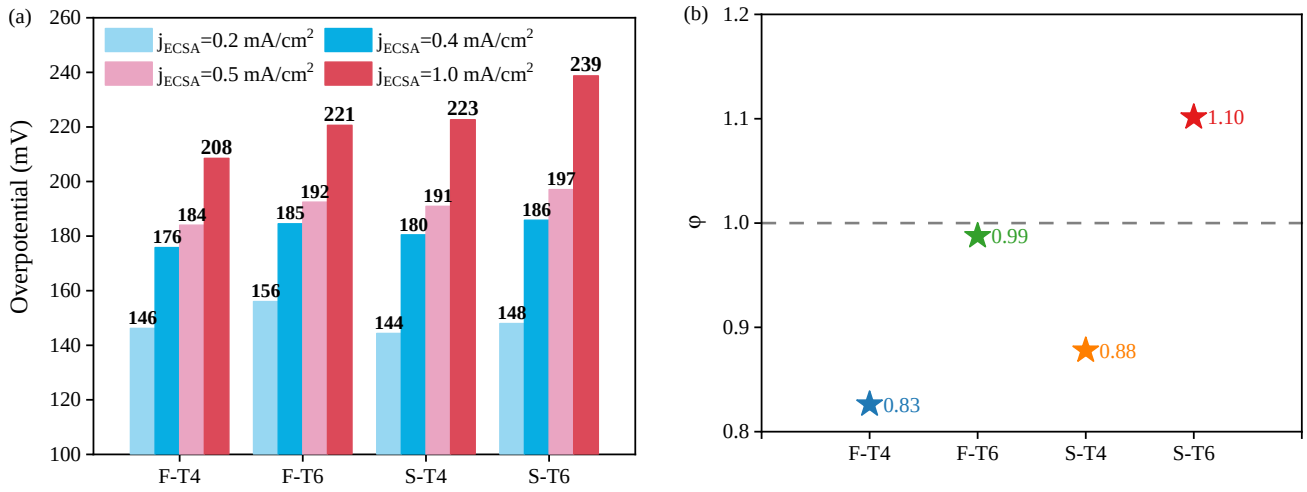

Fig. 5. (a) Overpotential at different j_{ECSA} forelectrodes; (b) the value of φ with different aligned porous electrodes

the reaction dynamics, the difference between $\Delta\eta_1$ and $\Delta\eta_2$ reflects the effect of bubbles. Define φ as the ratio of $\Delta\eta_2$ to $\Delta\eta_1$ ($\varphi = \Delta\eta_2 / \Delta\eta_1$), the value of φ represents the change between the overpotential caused by the bubble in the high current density range and the low current density range. In practical process, $\varphi < 1$ indicates that the overpotential caused by bubbles is smaller at high current density. And $\varphi > 1$ indicates that the overpotential caused by bubbles is smaller at low current density. According to Faraday law, as the current density increases, the rate of bubble generation also increases. If the electrode cannot remove the bubbles in time, the accumulated bubbles will significantly contribute to the overpotential. Hence, the value of φ serves as an indicator of the bubble removal capability of the electrode.

Fig. 5b shows the values of φ for each electrode. It can be observed that the φ value increases with the electrode thickness increase, indicating a weakening capability of bubble removal for thicker electrodes. Additionally, the bubble removal capability of the aligned porous electrode prepared by spherical nickel powder exhibits a weaker bubble removal capability compared to the one prepared with flake nickel powder. This difference can be attributed to the skeleton formed by the accumulation of nickel powder particles. In the case of spherical nickel powder, the resulting skeleton possesses more derivatives, and the mean pore size is smaller, which increases the resistance of bubble transmission. On the other hand, with flake nickel powder, fewer skeleton derivatives are formed and the average pore diameter is larger, resulting in a smoother surface for the skeleton formed by the accumulation of flake nickel powder, which promotes the transportation of bubbles.

4. CONCLUSIONS

This study investigates the difference of hydrogen evolution performance of aligned porous electrodes prepared using different morphology of nickel powder. The results demonstrate that the aligned porous electrode prepared by spherical nickel powder exhibits low overpotential at low current density primarily due to its larger ECSA. The dense porous skeleton formed by the accumulation of spherical nickel powder has more derivatives and a rougher surface, which hinders the transport rate of bubbles. In contrast, the skeleton formed by flake nickel powder is smoother. Consequently, as the current density increases, the overpotential of the aligned porous electrode prepared with spherical nickel powder becomes greater than that of the electrode prepared with flake nickel powder.

On the other hand, the aligned porous electrode prepared by flake nickel powder demonstrates better hydrogen evolution performance and higher material utilization rate at high current density. Additionally, the hydrogen evolution performance of the electrode further improves with increasing thickness.

ACKNOWLEDGEMENT

There is no funding for this study.

DECLARATION OF INTEREST STATEMENT

The authors declare that they have no known competing financial interests or personal relationships that could have appeared to influence the work reported in this paper. All authors read and approved the final manuscript.

REFERENCE

[1] van Leeuwen C, Mulder M. Power-to-gas in electricity markets dominated by renewables. Applied Energy. 2018;232:258-72.

[2] Colbertaldo P, Guandalini G, Campanari S. Modelling the integrated power and transport energy system: The role of power-to-gas and hydrogen in long-term scenarios for Italy. Energy. 2018;154:592-601.

[3] Lewandowska-Bernat A, Desideri U. Opportunities of power-to-gas technology in different energy systems architectures. Applied Energy. 2018;228:57-67.

[4] Mazza A, Bompard E, Chicco G. Applications of power to gas technologies in emerging electrical systems. Renewable and Sustainable Energy Reviews. 2018;92:794-806.

[5] Bailera M, Peña B, Lisbona P, Romeo LM. Decision-making methodology for managing photovoltaic surplus electricity through Power to Gas: Combined heat and power in urban buildings. Applied Energy. 2018;228:1032-45.

[6] Grueger F, Möhrke F, Robinius M, Stolten D. Early power to gas applications: Reducing wind farm forecast errors and providing secondary control reserve. Applied Energy. 2017;192:551-62.

[7] Mohammadi A, Mehrpooya M. A comprehensive review on coupling different types of electrolyzer to renewable energy sources. Energy. 2018;158:632-55.

[8] Götz M, Lefebvre J, Mörs F, McDaniel Koch A, Graf F, Bajohr S, et al. Renewable Power-to-Gas: A technological and economic review. Renewable Energy. 2016;85:1371-90.

[9] Wang M, Wang Z, Gong X, Guo Z. The intensification technologies to water electrolysis for hydrogen production – A review. Renewable and Sustainable Energy Reviews. 2014;29:573-88.

[10] Yuan S, Zhao C, Cai X, An L, Shen S, Yan X, et al. Bubble evolution and transport in PEM water electrolysis: Mechanism, impact, and management. Progress in Energy and Combustion Science. 2023;96.

[11] Sullivan I, Zhang H, Zhu C, Wood M, Nelson AJ, Baker SE, et al. 3D Printed Nickel-Molybdenum-Based Electrocatalysts for Hydrogen Evolution at Low Overpotentials in a Flow-Through Configuration. ACS Appl Mater Interfaces. 2021;13:20260-8.

[12] Liu H-b, Hu Q, Pan L-m, Wu R, Liu Y, Zhong D. Electrode-normal magnetic field facilitating neighbouring electrochemical bubble release from hydrophobic islets. Electrochimica Acta. 2019;306:350-9.

[13] Baczyzmalski D, Karnbach F, Mutschke G, Yang X, Eckert K, Uhlemann M, et al. Growth and detachment of single hydrogen bubbles in a magnetohydrodynamic shear flow. Physical Review Fluids. 2017;2.

[14] Ming-Yuan Lin W-NH, Lih-Wu Hourng, Teng-Shih Shih, and Chien-Ming Hung. Effect of Lorentz Force on Hydrogen Production in Water Electrolysis Employing Multielectrodes 2016.

[15] Cho KM, Deshmukh PR, Shin WG. Hydrodynamic behavior of bubbles at gas-evolving electrode in ultrasonic field during water electrolysis. Ultrason Sonochem. 2021;80:105796.

[16] Li S-D, Wang C-C, Chen C-Y. Water electrolysis in the presence of an ultrasonic field. Electrochimica Acta. 2009;54:3877-83.

[17] Zhang Z, Wu Y, Zhang D. Potentiostatic electrodeposition of cost-effective and efficient Ni–Fe electrocatalysts on Ni foam for the alkaline hydrogen evolution reaction. International Journal of Hydrogen Energy. 2022;47:1425-34.

[18] Liu W, Xia T, Ye Y, Wang H, Fang Z, Du Z, et al. Self-supported Ni3N nanoarray as an efficient nonnoble-metal catalyst for alkaline hydrogen evolution reaction. International Journal of Hydrogen Energy. 2021;46:27037-43.

[19] Guo J, Wei Z, Wang K, Zhang H. Synergistic coupling of CoFe-layered double hydroxide nanosheet arrays with reduced graphene oxide modified Ni foam for highly efficient oxygen evolution reaction and hydrogen evolution reaction. International Journal of Hydrogen Energy. 2021;46:27529-42.

[20] Qiu Y, Zhang X, Han H, Liu Z, Liu J, Ji X. Advantageous metal-atom-escape towards super-hydrophilic interfaces assembly for efficient overall water splitting. Journal of Power Sources. 2021;499.

[21] Yeon JS, Gupta N, Bhattacharya P, Park HS. A New Era of Integrative Ice Frozen Assembly into Multiscale Architecturing of Energy Materials. Advanced Functional Materials. 2022.

[22] Shao G, Hanaor DAH, Shen X, Gurlo A. Freeze Casting: From Low-Dimensional Building Blocks to Aligned Porous Structures-A Review of Novel Materials, Methods, and Applications. Adv Mater. 2020;32:e1907176.

[23] Zu L, Wu J, Liu X, Zhang L, Zhou K. Porous NiCu alloy with tailored pore structure and mechanical property fabricated by freezing casting. Materials Research Express. 2017;4.

[24] Scotti KL, Dunand DC. Freeze casting – A review of processing, microstructure and properties via the open data repository, FreezeCasting.net. Progress in Materials Science. 2018;94:243-305.

[25] Liu R, Xu T, Wang C-a. A review of fabrication strategies and applications of porous ceramics prepared by freeze-casting method. Ceramics International. 2016;42:2907-25.
[26] Liu X, Wu J, Luo B, Zhang L, Lai Y. Porous Cu foams with oriented pore structure by freeze casting. Materials Letters. 2017;205:249-52.
[27] Xiao F, Li L, Cui W, Zhang Y, Zhan C, Xiao W. Aligned porous nickel electrodes fabricated via ice templating with submicron particles for hydrogen evolution in alkaline water electrolysis. Journal of Power Sources. 2023;556.